Industrial Solar Drying System: Modeling and Design Optimization of Plate Slotted Fin-and-Tube Heat Exchanger

M. Bououd[*‡], A. Mechaqrane[*], K. Janusevicius[**], V. Martinaitis[**]

* Renewable Energies and Intelligent Systems Laboratory, Electrical Engineering Department, Faculty of Sciences and Technology, Sidi Mohammed Ben Abdellah University, PO. Box 2202, Fez, Morocco

** Laboratory of Building Energy and Microclimate Systems, Building Energetics Department, Faculty of Environmental Engineering, Vilnius Gediminas Technical University, Saulėtekio al.11, Vilnius, Lithuania.

(Mahmoud.bououd@usmba.ac.ma, Abdellah.mechaqrane@usmba.ac.ma, karolis.janusevicius@vgtu.lt, vytautas.martinaitis@vgtu.lt)

‡ Corresponding Author; Mahmoud Bououd, FST de Fès, Route d'Imouzzer, PO. Box 2202, Fez, Morocco,

Tel: + 201205881264, Mahmoud.bououd@usmba.ac.ma

Received: 05.02.2019 Accepted:25.03.2019

Abstract- Drying is one of the most energy-intensive stages in clay bricks manufacturing where fuel or another conventional energy source is used to heat the air before blowing it on the wet bricks. In order to reduce the energy consumption and decrease the carbon footprint of construction materials, thermal solar heat represents a promising and suitable energy source for this industrial application. In this paper, the utilization of solar energy in clay bricks drying process through compact cross flow water-to-air heat exchanger is investigated. Considering the intermittent profile of solar radiations, modeling and experimental validation of a water-to-air heat exchanger thermo-flow characteristics estimation at variable hot fluid temperature is performed. An agreement of more than 97% between numerical results and experimental measurements is demonstrated. Additionally, in order to improve the industrial solar drying system efficiency, an optimization of the heat exchanger geometric parameters is carried out based on the performance evaluation criterion and the required drying temperature in clay bricks manufacturing. According to findings, the recommended configuration for a constant heat transfer volume of 0.05 m^3 is characterized by tube diameter, longitudinal and transverse pitches of 18 mm, fin spacing of 2.9 mm and fin thickness of 0.6 mm. This configuration is able to increase the heat exchanger performance evaluation criterion by around 53% compared to the baseline configuration. The annual thermal performance of the solar dryer is evaluated via dynamic simulation via the TRNSYS software and shows that the optimal configuration improves the drying temperature by more than 16%.

Keywords Industrial solar drying, Slotted Fin-and-tube heat exchanger, Design Optimization, Thermo-flow characteristics.

1. Introduction

By definition, drying is the process of excess moisture removal from a natural or an industrial product to preserve it or reach the required water content level.
Drying is an energy-intensive process in several industries such as textiles, phosphate, dairy processing, production of cement, wastewater treatment, production of tiles and clay bricks, etc.

Two processes take place in drying: (i) the heat transfer to the product using energy from the heating source, and (ii) the mass transfer of moisture from the interior of the product to its surface and from the surface to the surrounding air, in the form of water vapor [1].

The industrial drying process represents, on average, 12% of the total energy consumption in manufacturing process, which is estimated to be more than 10^{11}MJ/year in industrialized countries. Furthermore, the specific heat energy consumption in the brick industry is, on average, 2.18 MJ/kg brick [2, 3].

Drying is an essential stage in clay bricks industry due to the unsuitable properties and characteristics of raw clay to produce the requested quality of bricks. When the ground clay is mixed with water, its plasticity allows it to be shaped as required. Eight main operations are conducted in the clay bricks manufacturing process; this includes mining, storage, size reduction, screening, cutting, coating or glazing, drying, firing and cooling. After the coating stage, the bricks contain between 7% and 30% of water, depending on the forming method. The bricks must be dried at a temperature between 311.15 K and 477.15 K during a time range from 24 to 48 h [4].

Generally, the required energy for this process could be provided by several sources such as, electricity, fossil fuels, natural gas, wood and solar radiation. In fact, this last renewable energy source has been used in drying stage of several manufacturing processes such as the food, breweries, tobacco, textile and chemical industries [5]. Different solar collector technologies have been considered in industrial sectors based on the required drying temperature. Table 1 illustrates the main industries where solar dryers are currently installed as well as the used solar collectors along with their respective drying temperature range. It can be noticed that no industrial solar drying system for clay bricks manufacturing has been identified by the International Energy Agency (IEA) in the framework of the IEA Task 49/IV.

Furthermore, several research attempts on solar drying system utilization in the industrial sector have been reported in the literature. The design consideration and calculation results of a constructed solar dryer for a mango factory were presented. This solar dryer was used to dry thin layers of mango slices from about 81.4 % moisture content (wet basis) to 10% (wet basis) in 20 hours [6]. The performance of a solar dryer used for sludge drying from pharmaceutical industrial waste was experimentally evaluated, and demonstrated that the solar sludge drying sand bed reduced drying time by about 25-35% when compared to the conventional sludge drying sand bed [7]. Rural Industries Research and Development Corporation has developed a new solar drying machine for agricultural products using dry air rather than heated air for grains and seeds drying process [8]. The involved researchers have concluded that LiCl is a very effective desiccant and estimated that over 50% savings in energy cost are achievable. The fundamentals and literature on solar drying and solar air heating systems was explored. One of the main recommendations of this review paper is the utilization of computer simulation models in solar drying systems performance assessment [9].

Nomenclature

A	heat transfer surface area (m^2)	Re	air side Reynolds number
A_b	base surface area (m^2)	Re_w	water side Reynolds number
A_f	fins surface area (m^2)	r_c	tube outside radius, including collar thickness (m)
A_c	minimum free flow area (m^2)	R_{eq}	equivalent radius for circular fin
c_p	specific heat (J/kg K)	S_T	transverse pitch (m)
D	external tube diameter (m)	S_L	longitudinal pitch (m)
D_i	internal tube diameter (m)	S_D	diagonal pitch (m)
D_h	hydraulic diameter (m)	T_w	surface temperature (K)
F_s	fin spacing (m)	T_i	inlet temperature of air (K)
f	air side friction factor	T_o	outlet temperature of air (K)
f_w	water side Friction factor	ΔT_{lm}	log-mean temperature difference (K)
j	Colburn factor	V	air velocity (m/s)
h	convective heat transfer coefficient ($W/m^2.K$)	U_m	maximum air velocity in the minimum flow area (m/s)
L	total tubes length (m)	U_w	water velocity (m/s)
M_{air}	air mass flow rate (kg/s)		
Nu	air side Nusselt number		
Nu_{lam}	water side Nusselt number in laminar flow regime	***Greek symbols***	
Nu_{turb}	water side Nusselt number in turbulent flow regime	α	fin oblique angle (°)
Nu_{tra}	water side Nusselt number in transitional flow regime	δ	fin thickness (m)
N_T	number of tubes per row	λ	air thermal conductivity (W/m.K)
N_L	number of rows	ρ	air density (kg/m^3)
N	total tubes number	ρ_w	water density (kg/m^3)
n_f	number of fins	μ	average free-stream viscosity, ($N.s/m^2$)
Pr	water side Prandlt number	μ_w	water dynamic viscosity ($N.s/m^2$)
P_c	perimeter at the minimum flow cross-section (m)	γ	distance between laminar and turbulent flow regimes
Δp	air pressure drop (Pa)	ζ_f	fin efficiency

Δp_w	water pressure drop (Pa)	λ_f	fin conductivity (W/m.K)

Table 1: Current installed industrial solar drying systems [38]

Industry	Country	Name	Industrial Operation	Solar Collector	Drying Temperature (°C)
Breweries	Germany	Newmarketer Lammsbraw	Drying process	Air collector	~60
Food	USA	Keyaqa Orchards	Walnuts Drying	Air collector	~43
		Kreher's Poultry Farms	Drying of chicken Eggs	Air collector	-
		Stapleton Spence Fruit Packing Co.	Rehydrate Dried Foods	Unglazed collector	-
		Sunsweet Dryers	Prune Drying	Air collector	10 ~ 15
		Carriers & Sons	Walnuts Drying	Air collector	~43
	India	Kaveri Agricare Pvt. Ltd.	Drying Coir Peat	Air collector	~ 105
	Costa Rica	Coopeldos	Coffee Drying	Air collector	40 ~ 45
	Panama	Duren Coffee	Coffee Drying	Air collector	40 ~ 45
	China	Fengli Fruit Drying	Fruit Drying	Air collector	50 ~ 70
	Indonesia	Malabr Tea Drying	Tea Drying	Air collector	~ 35
Mining	Austria	Korner Kvk	Preheating, drying	Flat plat collector	50 ~ 80
Agriculture	India	AMR dal Mill	Drying of Pulse	Air collector	65 ~ 75
	Romania	Aroma Plant Romania	Drying of Medicinal Plants	Air collector	-
	Romania	Hofigal S.A.	Drying of medicinal plants, herbs and fruits	Air collector	-
	USA	Sonoma Country Herb Exchange	Drying of Herbs	Air collector	-
	Germany	Krimmer	Drying of Wild Flower Seeds	Flat plate collector	-
	Mexico	ZACATECAS TERMOSOLAR DRYING PLANT	Drying agricultural products	Air collector	55 ~ 120
				Flat plat collector	70 ~ 85
Leather	India	Leo Leather	Chemical mixing, drying	Flat plate collector	-
Fabricated Metal	Germany	Lackiercenter Shulte	Drying Chamber	Evacuated tube collector	-
	Portugal	Silampos S.A.	Drying finished product	Parallel trough collector	50–160
Tobacco	Argentina	Grammer Solar Argentina	Drying of tobacco	Air collector	-
Rubber & Plastic Products	Thailand	Inter Rubber Latex Co. Ltd.	Drying of natural rubber	Air collector	-
Concrete	Austria	Leitt Beton Gmbh	Drying of pre-fabricated concrete components	Flat plate collector	-
Furniture	Austria	Carpenting Hamminger	Wood Drying	Flat plate collector	25–115
Repairing & Installation	Germany	Lackiererei Vogel	Drying process	Evacuated tube collector	22–24, 60–70
Textile	USA	Acme McCrary	Textile Drying	Flat plate collector	-

Transporting and storage	Germany	Kölner VKB	Drying process	Evacuated tube collector	~ 70
Waste management	USA	Rockland County	Waste drying	Air collector	-
Chemical	India	Ultramarine Pigments	Drying of pigments	Paraboloid dish	~ 140

Solar drying system for agricultural industry with a CPC evacuated tubular solar collector was constructed and the system's performance with indoor and outdoor drying was compared. The considered solar dryer has shown better performances by reducing the drying time by half for all studied samples [10]. The development of solar energy applications in industrial sector from multiple viewpoints was discussed [11]. This study suggested the exploration of solar drying systems for industrial purposes based on energy and exergy analysis. In order to identify obstacles and barriers facing solar drying utilization in the industrial sector, authors recommended to conduct further comprehensive studies and investigations on this research topic. The drying kinetics of fresh species were described and the solar energy was approved as a suitable source or drying processes [12]. Different types of solar dryers for agricultural products were reviewed with particular focus on environmental impact. Additionally, the best solutions to overcome the issues related to traditional drying have been explored [13]. The thermal performance of flat plate solar dryer for large scale carpet industry was evaluated. The obtained experimental results showed that 320 kg of wet wool and carpet could be dried in 7.5 hours under an average solar irradiation intensity of 800 W/m^2, and an average solar air field thermal efficiency of 48% [14]. Solar drying for the three main wastes from the olive oil industry was investigated and the analysis enabled further knowledge about the drying kinetics and the obtained results were extrapolated to large scale solar drying systems [15]. Development directions of solar dryers in China were explored by reviewing 5 types of solar energy systems used in herbal Chinese medicine drying process. The authors concluded that the improvement of vacuum tube collector efficiency will enhance the final product quality [16]. The progress in different solar dryer types through various applications was reviewed. This investigation suggested the optimization of each stage in solar drying process for better techno-economic feasibility, and it also highly recommended to model and simulate the solar dryer thermal performance before scaling up the system [17]. A small-scale solar drying system for clay tiles was designed and its thermal performance was evaluated using a dynamic simulation environment (Trnsys). Additionally, the solar drying system components were optimized according to the variation of the material's moisture content [18]. The performances of three different solar drying systems for Tunisian phosphate namely open to sun, greenhouse and parabolic dish concentrator were compared based on the obtained residual phosphate moistures and drying periods. The researchers demonstrated that solar drying using parabolic dish concentrator gives better results compared to the two other systems [19].

According to this literature review, a clear lack of studies, dealing with solar energy deployment in clay brick drying process is noticeable. This last outcome is one of the factors that has encouraged us to explore the possibility of using solar drying systems in this industrial sector. Moreover, the relatively high required operating temperature is another limitation facing the utilization of the commonly used solar collectors such as air collectors, flat plate collectors or evacuated solar collectors in clay bricks drying process. Therefore, and in order to efficiently reach the required drying temperatures, the solar dryer components' design has to be optimized based on the specific external parameters for industrial drying. The main components of our proposed solar dryer are evacuated tube solar collector, storage tank and water to air heat exchanger.

The present paper deals with heat transfer modeling and design optimization of four-row slotted plate finned heat exchanger of an industrial clay bricks solar dryer. Indeed, one of the key factors in improving the efficiency of solar energy systems is the design optimization of heat exchange devices [20].

The compact cross flow heat exchanger is one of the most effective devices and widely implemented for heat recovery in a variety of engineering applications due to its numerous advantages, such as the large amount of heat that can be transferred from a small exchange area, the simplicity of design and manufacturing, wide operating temperature ranges and the control ability of high heat flow rate at different temperature levels [21]. Generally, tubes are mechanically or hydraulically expanded in a block of parallel continuous fins to manufacture finned tube heat exchangers that can be produced with one or more rows according to the application requirements. In order to improve the flow disturbance and, consequently, the thermo-flow performance of the tube bundles, different fin patterns have been developed (e.g. plain, slot, dimples, wavy, louver and convex-louver). Additionally, geometric parameters of the finned tube bundles, such as fin pitch, fin thickness, number of tube rows, transverse and longitudinal pitches, tube type and tube arrangement, play a significant role in the thermo-flow performance enhancement.

Several studies have been performed based on experimental and numerical investigations to explore the ability of slotted fin-and tube bundle to break and renew the thermal boundary layer which enhances the convection heat transfer performances. Slotted fins become more attractive for many researchers because of their heat transfer enhancement and relatively low pressure drop penalty. Numerical simulation was performed to compare two-row plain fins and three other types of radial slotted fins. It has been shown that at the same frontal air velocity (1-3m/s) the heat transfer rate and pressure losses of the full slotted fin are superior to that of the plain plate [22]. The geometric configuration for a two-dimensional slotted fin was optimized through genetic algorithm coupled with numerical simulation. At an air side Reynolds number Re=500, the results showed that the flow area goodness factor *j/f* increases by 11.11% based on optimal

integrated performance $(j/j_0)/(f/f_0)$ while the Colburn factor j is increases by 479.08% based on optimal heat exchange capacity j/j_0 [23]. The heat transfer and fluid flow characteristics of two slotted fin surfaces X-type and arc-type were numerically investigated. It has been pointed out that the X-type fin surface has the highest heat transfer performance and pressure drop. The study suggested an improved slotted fin surface (Butterfly-type) which increase heat duty by 20-24% and reduce pumping power by 38-51% [24]. The effects of continuous and alternant rectangular slots on the thermo-flow performance for staggered and in-line alignments were numerically investigated. The simulations showed that the staggered fin-and-tube bundles with continuous slotted rectangular strips have best overall performance [25]. Additionally, and according to another numerical investigation, the thermo-flow characteristics analysis of different fin-and-tube bundles showed that slotted fin pattern provides higher thermal-aerodynamic performances [26].

According to the above overview, it can be noticed that plate alternant slotted fins are one of the most effective patterns that improve the tube bundles' performances. Additionally, geometric parameters of the tube bundles such as tubes diameter, transverse and longitudinal pitches, fins spacing and fins thickness have a major impact on the thermal and aerodynamic performances of the heat exchanger.

The paper is organized as follows. At first, physical models for both water and air sides are described based on suitable correlations of Nusselt number and friction factor. Afterwards, the reliability of the considered models at variable hot fluid temperature is experimentally investigated. Finally, the heat exchanger design optimization is conducted and the solar drying system thermal performance is evaluated for the optimal tube bundles configuration via the dynamic simulation software (TRNSYS).

2. Physical Model

2.1. Water side flow and heat transfer models

In this section, the water side pressure drop and heat transfer characteristics are described based on widely accepted models. Following part details mathematical models presented and used in reliable sources [26-28]. These expressions are used to define overall heat transfer coefficient and pressure drop of water side heat exchanger. The pressure drop in pipe flow is given by the following equation [27]:

$$\Delta P_w = \frac{1}{D_i}\frac{\rho_w U_w^2}{2} f_w \tag{1}$$

Velocity in pipes is expressed by basic function [27]:

$$U_w = \frac{\pi(\rho_w M_w)^2}{4} \tag{2}$$

In order to calculate friction factors for flow inside of the pipe, the Reynolds number is required. The expression of this non-dimensional number expressing ratio between viscous and friction forces is defined by the following formula [27]:

$$Re_w = \frac{U_w \rho_w D_i}{\mu_w} \tag{3}$$

In the cases when flow is turbulent, various expressions exist. The roughness of the tube wall is an important factor. The only surfaces for which an accurate rule can be quoted for the resistance are those that are technically smooth [27]. Much greater resistances to flow are encountered if the surfaces are rough; it depends solely on the roughness in turbulent flow, but, in the transition zone, it also depends on the Reynolds number. The numerous observations that have been made have failed to establish a general relationship between pressure drop and roughness that would embrace the multiplicity of cases that are likely to occur in practice [27, 28]. Haaland equation [28] is used for this case, because there is no need to iterate the Darcy friction factor like in other expressions [27]. The accuracy of the Darcy friction factor solved from this equation is claimed to be within about ±2 %, if the Reynolds number is above 3000. The friction factor is expressed as follows [27]:

$$f_w = \frac{1}{\left(-1.8\log\left(\left(\frac{6.9}{Re_w}\right) + ((k/D_i)/3.71)^{1.11}\right)\right)^2} \tag{4}$$

Friction factor is dependent on flow regimes. For the cases when internal flow is laminar and internal pipe surface can be assumed to be smooth, the friction coefficient is calculated by the formula [27]:

$$f_w = \frac{Re_w}{64}$$

By using given equations 4 and 5, pressure drop in water side is determined for both laminar and turbulent cases.

The heat transfer coefficient, used to define heat flux from water side, is expressed from Nusselt number, which is calculated for the case of laminar forced internal flow and fully developed turbulent flow. In the laminar flow regime, Nusselt number remains constant and could be assumed equal to [27]:

$$Nu_{lam} = 3.6567 \tag{6}$$

While in the flow which is highly turbulent, heat transfer intensity depends on Reynolds and Prandtl numbers and friction factor (with all other relations associated to friction factor). These dependencies could be summarized and expressed by the equation suggested by Gnielinski et al [27]:

$$Nu_{turb} = \frac{(f_w/8)Re_w Pr}{1 + 12.7\sqrt{\frac{f_w}{8}}(Pr^{2/3} - 1)}\left[1 + \left(\frac{D_i}{l}\right)^{2/3}\right] \tag{7}$$

The heat exchanger may operate in cases other than during laminar or fully developed turbulent flow in the water side. For the cases when flow regime falls between Re > 2300 and Re < 10^4, the heat transfer coefficient should be expressed

from transitional flow approximation suggested by Gnielinski et al [27]:

$$Nu_{tran} = (1-\gamma)Nu_{lam} + \gamma Nu_{turb} \quad (8)$$

In order to describe the temporal sequences, the intermittency factor γ is expressed as follows [27]:

$$\gamma = \frac{Re_w - 2300}{10^4 - 2300} \; and \; 0 \le \gamma \le 1 \quad (9)$$

Where $\gamma = 1$ if the flow is permanently turbulent, and $\gamma = 0$ if the flow is permanently laminar.

The above described physical model allows to examine heat transfer intensity in a wide range of water side flow rates and can be employed for optimization tasks.

1.1. Air side flow and heat transfer models

1.1.1. Parameters definition

The modeling of thermo-flow characteristics of the slotted finned tubes heat exchanger (Fig.1) is performed based on the following assumptions:

- Steady-state flow
- Incompressible fluid
- Neglected radiation effect
- Constant thermo-physical properties of the solid and fluid.

The heat transfers on the air side of the finned tube bundles in staggered configuration (Fig. 2) is modeled based on the following dimensionless parameters [30, 31]:

The Reynolds Number:

$$Re = \rho U_m D/\mu \quad (10)$$

with:

$$U_m = \begin{cases} U(S_T/2a) \;\; if \; 2a \le 2b \\ U(S_T/2b) \;\; if \; 2a \ge 2b \end{cases} \quad (11)$$

where ρ and μ are the density and dynamic viscosity respectively, estimated at the mean inlet temperatures.
2a and b are shown in Fig. 3 and could be calculated based on the geometric parameters as follow:

$$2a = (S_T - D) - \left[(S_T - D)\delta . n_f\right] \quad (12)$$

$$b = (S_D - D) - \left[(S_T - D)\delta . n_f\right] \quad (13)$$

The friction factor is:

$$f = 2\,\Delta p/\rho U_m^2 \quad (14)$$

Δp is the pressure drop across the finned tube bundles.

The Nusselt Number is:

$$Nu = h\,.D/\lambda \quad (15)$$

where λ is the air thermal conductivity and h is the average heat transfer coefficient which is defined by:

$$h = \Phi/A\,\Delta T \quad (16)$$

where Φ is the total heat flow rate calculated by:

$$\Phi = M_{air} C_p (T_o - T_i) \quad (17)$$

and A is the heat transfer surface area estimated by:

$$A = A_b + \zeta_f A_f \quad (18)$$

where A_b is the area of the base surface and A_f is the area of the fins.

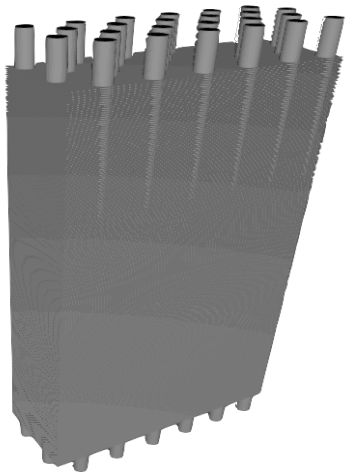

Fig. 1: Architecture of the finned tubes heat exchanger

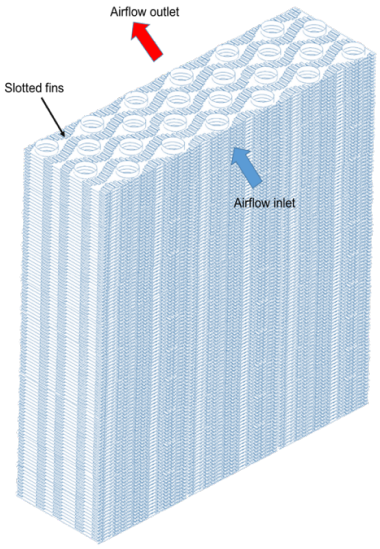

Fig.2: Schematic diagram of slotted finned tube bundles in staggered configuration

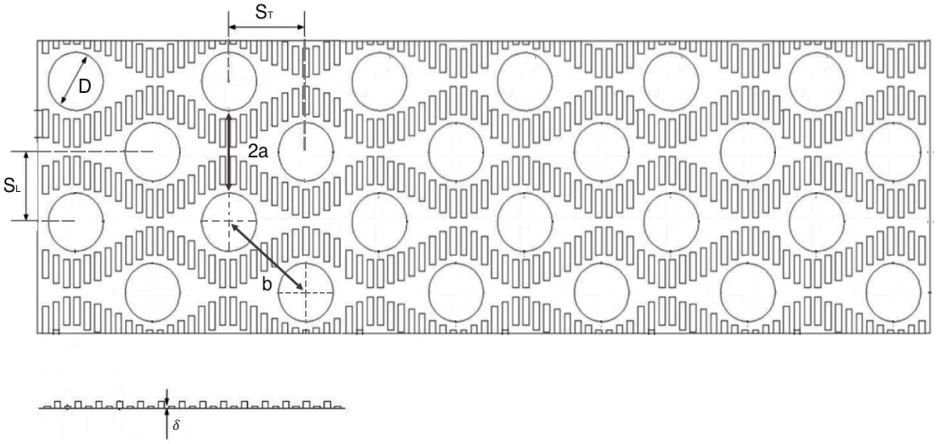

Fig. 3: Schematic diagram of geometric parameters

The approximation method defined by Schmidt [29] estimates the fin efficiency ζ_f by the following correlation:

$$\zeta_f = \frac{\tanh(mr_c\phi)}{mr_c\phi} \tag{19}$$

where

$$m = \sqrt{\frac{2h}{\lambda_f \delta}} \tag{20}$$

$$\phi = \left(\frac{R_{eq}}{r_c} - 1\right)\left[1 + 0.35log_e\left(\frac{R_{eq}}{r_c}\right)\right] \tag{21}$$

$$\frac{R_{eq}}{r_c} = 1.27\frac{X_M}{r_c}\left(\frac{X_L}{X_M} - 0.3\right)^{0.5} \tag{22}$$

$$X_M = S_T/2 \tag{23}$$

$$X_L = \sqrt{{X_M}^2 + {S_L}^2/2} \tag{24}$$

The logarithmic mean temperature difference between the tube wall and the air is defined as:

$$\Delta T = \frac{(T_w - T_i) - (T_w - T_o)}{ln(T_w - T_i/T_w - T_o)} \tag{25}$$

1.1.2. Nusselt number and friction factor correlations

In order to enable thermo-flow performances prediction and heat exchangers design, several correlations have been established in the literature based on experimental and computational studies for different numbers of row and fin patterns. Most of the conducted investigations allow for the estimation of the average heat transfer coefficient and the pressure drop through the calculation of the Nusselt number and the friction factor respectively (based on geometric parameters of finned tube bundles).

Kong et al [26] have established correlations for four-rows alternant slotted finned tube bundles based on a three dimensional simulation validated by experimental tests. The correlations were developed using multiple linear regression analysis in function of longitudinal and transverse pitches as well as tube diameter. The air side friction factor and Nusselt number are expressed as follows:

$$f = 324.0431\, Re^{-0.4825}\left(\frac{S_T}{D}\right)^{-0.0258}\left(\frac{S_L}{D}\right)^{-0.2419} \tag{26}$$

$$Nu = 4.8787\, Re^{0.3173}\left(\frac{S_T}{D}\right)^{-0.8571}\left(\frac{S_L}{D}\right)^{-0.6648} \tag{27}$$

with:

$$1 \le S_T/D \le 1.8\,,\quad 1 \le S_L/D \le 1.8\,,\quad 800 \le Re \le 13000$$

So as to estimate the overall performance of the finned tube bundles, the heat transfer capability of a surface with a given flow resistance, is commonly defined by the performance evaluation criterion P_{EC} which is calculated by the following equation [26]:

$$\mathrm{P_{EC}} = {\mathrm{Nu}}/{\mathrm{f}^{1/3}} \tag{28}$$

The required transmitted power to the air flow, to overcome pressure losses, can be estimated based on the following equation [19]:

$$W = \frac{M_{air}}{\rho}\,\Delta p \tag{29}$$

From the presented physical model of plate alternant slotted tube bundles, it can be noticed that the proposed correlations are fitted at constant hot fluid temperature since the considered conventional energy source is able to generate the hot fluid at constant temperature. Furthermore, due to the intermittency of solar energy, the heat exchanger performance estimation at variable hot fluid temperature is experimentally investigated in the next section, aiming to evaluate the reliability of the described physical model.

3. Experimental Validation

3.1. Experimental setup

An experimental validation of the thermo-flow performances of a 4-row alternant slotted finned tube heat exchanger (Fig. 4.a) has been performed using the experimental system presented in Fig. 5. The aim is to investigate the variation effect of the water inlet temperature on the heat exchanger performances prediction. The staggered configuration is characterized by transverse and longitudinal pitches of 35mm, diameter of 25mm, fin spacing of 3.2mm and fin thickness of 0.3mm, as schematically shown in Fig. 3. The heat exchanger's tubes and fins are made from aluminum, while the tube connections are made from resistant silicon to withstand high temperatures. The wind tunnel (Fig. 4.c) has a test section covered by asbestos layer to minimize heat losses that closely matches the experimental sample to eliminate the contraction and expansion losses. The test section size (Fig. 5) is 500mm width, 700mm height and 1000mm long. In the air loop, the flow rate is controlled by a digital blower speed controller able to provide an air velocity between 0.5 and 3.5m/s that is adjusted based on a hot wire anemometer with the precision of ±0.05m/s. Two strings of T-tubes has been implanted upstream and downstream of the exchanger to measure the pressure drop along the test section using an inclined single tube micro differential pressure gauge with a precision of ±0.15Pa. The water loop is supplied by a water temperature control system (Fig. 4.b) able to provide a constant flow of hot water at different temperatures up to 120°C in liquid phase guaranteed by an integrated pressure controller. The output of the water control system has been equipped by a turbine flow meter with a precision of ±0.14kg/s to control the water flow and keep it at 1kg/s during the experiments. Two T-type thermocouple grids have been implanted in the inlet (6 thermocouples) and outlet (24 thermocouples) of the test section. 12 T-type thermocouples have been implanted in the heat exchanger surface.

(a) (b) (c)

Fig. 4: Experimental facility for thermo-flow performance of slotted finned tube heat exchanger. (a)slotted finned heat exchanger sample,(b) water temperature control system, (c) wind tunnel experimental system

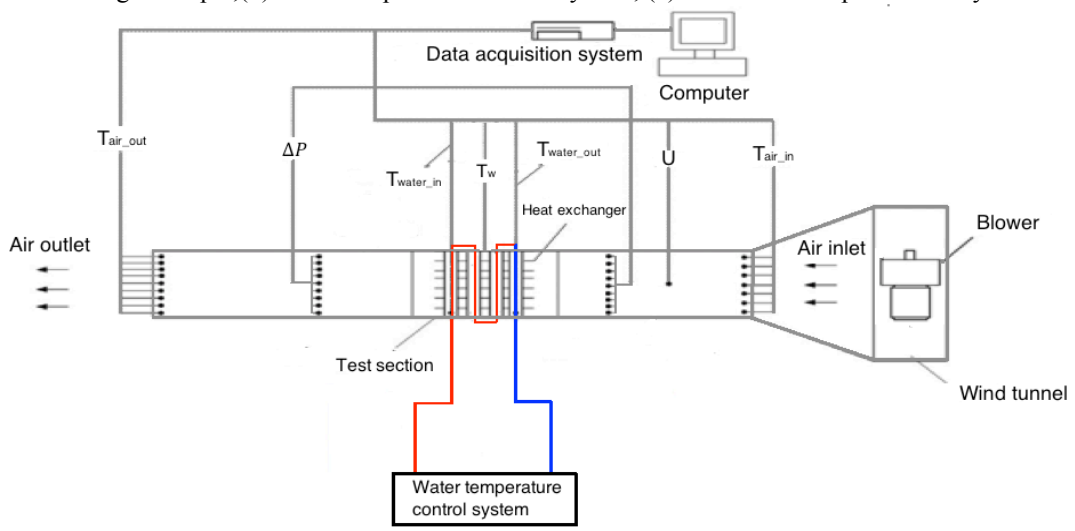

Fig. 5: Experimental setup and locations of measuring point

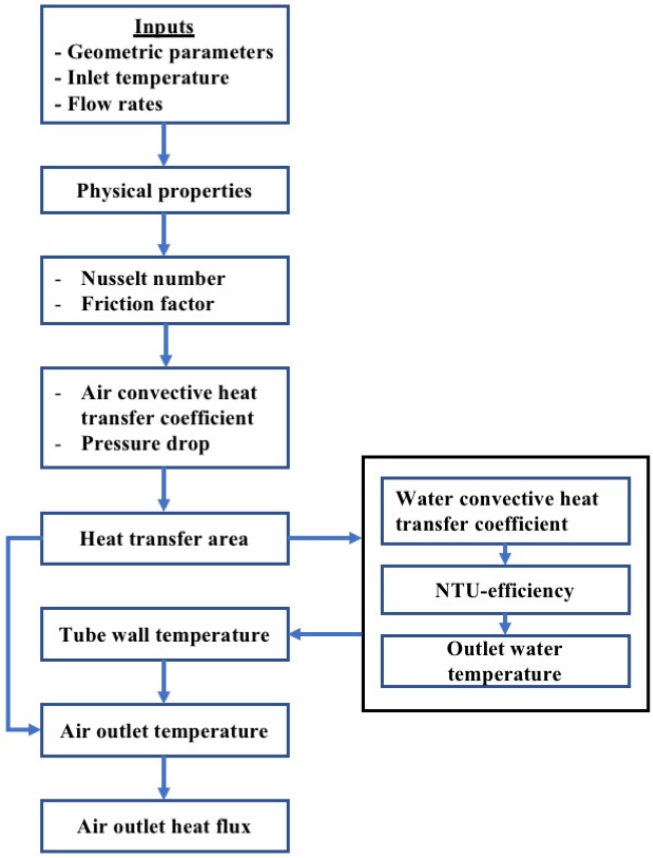

Fig. 6: Flow chart of computational code

Table 2: Maximum estimated uncertainties

Parameter	Measuring uncertainties (%)
m_{water}	3.98
u_{air}	4.33
T_{air_in}	0.22
T_{air_out}	0.53
T_{water_in}	0.17
ΔP	3.65
Re	4.71
Nu	6.82
f	6.37
h	6.81

In order to achieve accurate measurements, the thermocouples have been pre-calibrated using the ice point calibration method with an error range of ±0.1°C.
The thermocouple data was recorded by Agilent 34972A data acquisition system [32] and then averaged and collected by the host computer.

The uncertainty estimation in a computed result could be performed with good accuracy using a root-sum square combination of each of the individual independent variables $x_1, x_2, \dots, x_N$, when used in a function such as $\Gamma = f(x_1, x_2, \dots x_N)$. The basic equation of uncertainty analysis is estimated as follows [33]:

$$\delta\Gamma = \sqrt{\sum_{i=1}^{N} \left(\frac{\partial\Gamma}{\partial x_i}\right)^2 (\delta x_i)^2} \quad (30)$$

In this particular case, most of the equations describing the results are a pure product form such as Eq.30, then the relative uncertainty can be estimated directly. That is if

$$\Gamma = x_1^a x_2^b \dots x_N^m \quad (31)$$

Then

$$\frac{\delta\Gamma}{\Gamma} = \left[\left(a\frac{\delta x_1}{x_1}\right)^2 + \left(b\frac{\delta x_2}{x_2}\right)^2 + \dots + \left(m\frac{\delta x_N}{x_N}\right)^2\right]^{1/2} \quad (32)$$

where $x_1, x_2, \dots x_N$ are the measured variables used to calculate Γ and $\delta x_1, \delta x_2, \dots, \delta x_N$ are the tolerances of the corresponding variables.
Therefore, the estimated uncertainties of different experimental parameters are summarized in Table 2.

3.2. Model validation and analysis

The numerical estimation of the thermo-flow performance of four-row slotted fin-and-tube bundles has been conducted through a Matlab code, according to the presented flow chart in Fig. 6. The air and water flow rates as well as the air and water inlet temperatures are the inputs in the considered algorithm for thermo-flow characteristics calculations. Simulation results have been compared with experimental data to investigate the reliability of the proposed physical model in the estimation of the thermo-flow characteristics of the heat exchanger at variable hot water temperature between 323.15K and 363.15K.

The baseline parameters of the fin-and-tube bundles used in the numerical calculations are summarized in Table 3. In order to calculate the Nusselt number and friction factor based on the performed experimental measurements of the air outlet temperature and the pressure drop, the air thermal properties are evaluated at the mean temperature $(T_{air\ in} + T_{air\ out})/2$.

Based on the average temperatures, the primary measurements of the air outlet temperature, the heat exchanger surface temperature as well as the air pressure drop are represented versus the water inlet temperature and compared with numerical results in According to Fig. 7, it is noticed that maximum deviations of 0.26%, 0.61% and 2.9% occur between simulations and experimental data for air outlet temperature, surface temperature and air pressure drop respectively. Additionally, the air pressure drop decreases by around 4% when the inlet water temperature increases as it can be concluded from Fig. 7.c. This decrease in pressure loss can be explained by the rise of air pressure with the temperature in the outlet leading the decrease of the pressure drop for a constant air pressure in the inlet.

Despite the decrease of the pressure drop, it can be seen in Fig. 8.a that the friction factor has an increasing tendency with the water inlet temperature.

Table 3: Baseline parameters

Parameter	Value
$m_{water}\ (kg/s)$	1
u_{air} (m/s)	0.5
T_{air_in} (K)	289.15
$S_T = S_L$ (mm)	35
D (mm)	25
δ (mm)	0.3
F_s (mm)	3.2
N	24
N_L	4
n_f	214

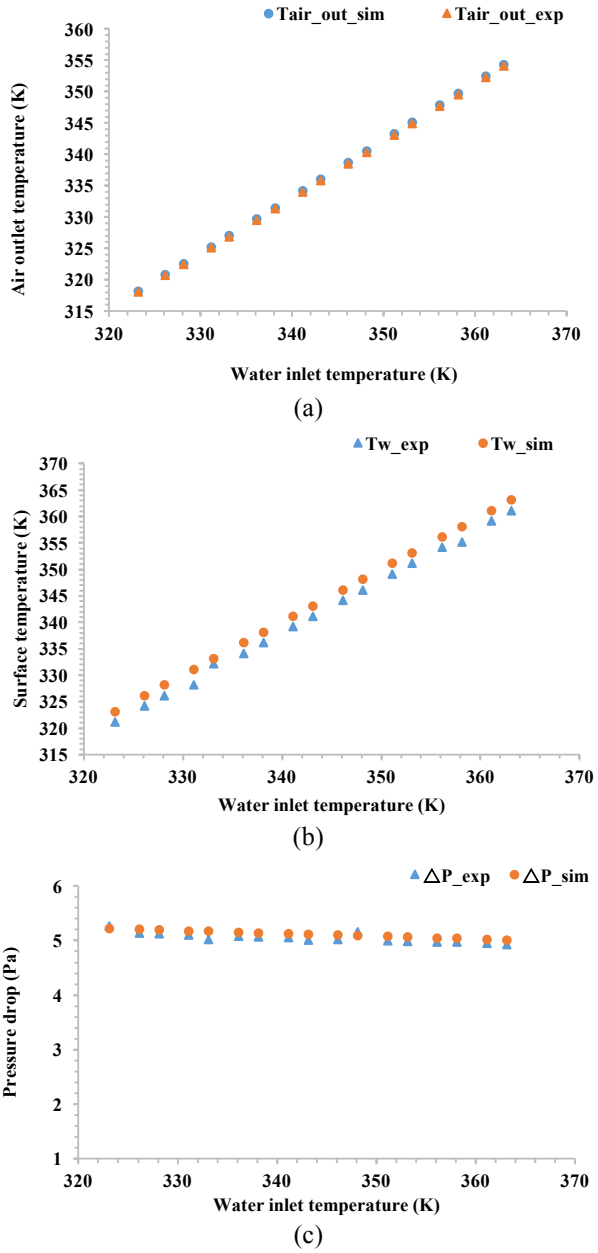

Fig. 7: Influence of water inlet temperature variation on (a) air outlet temperature (b) surface temperature and (c) air pressure drop

This can be explained by the increase in the air kinetic viscosity and the decrease of the air density with the temperature rise.

The derived parameters such as friction factor, Nusselt number and heat transfer coefficient are shown in Fig. 8. The comparison between simulations and experimental data illustrates that the maximum deviations are around 3.2%, 1.56% and 0.34% for friction factor, Nusselt number and heat transfer coefficient respectively. Nusselt number is decreasing with the increase of inlet water temperature as illustrated in Fig 8.b, which can be explained by the increase of the air kinetic viscosity with the temperature that consequently gives lower Reynolds number. Furthermore, the increase of the air conductivity with temperature leads to the enhancement of the convective heat transfer coefficient regardless of Nusselt number decline. It can be concluded from Fig. 7-8 that the predicted results agree. well with the experimental data for both heat transfer and fluid flow.

This shows the good reliability of the considered physical model and computational code allowing reliable estimation of the heat exchanger performances at variable inlet water temperatures and the optimization of different geometric parameters of the four-row slotted fin-and-tube bundles.

2. Design Optimization

Heat exchanger optimization is considered as a design process where all the design and operating parameters are evaluated based on the requirements (i.e. outlet temperature, pressure drop and heat flow rate). The most common objectives of heat exchanger optimization are the energy saving and resources conservation as well as capital and operating costs' reduction. In order to reduce the relatively high cost of solar energy conversion and consequently improve the solar drying system efficiency, a design analysis of the studied heat exchanger is conducted. The present parametric optimization aims to define the optimal geometric parameters and consequently improve the thermo-flow performances for a constant heat transfer volume of 0.05 m^3 and an air and water flow rates of, respectively, 0.171 kg/s and 1 kg/s.

The present parametric optimization is conducted with an inlet water temperature of 383.15K in order to meet the required air temperature in clay bricks drying that should be between 373.15 and 383.15K in the thermal room.

For the present optimization, the considered baseline parameters are listed in Table 3.

The investigation is performed based on the simultaneous variations of the geometric parameters (D, S_T, S_L, F_S, δ) for a constant heat exchanger volume of 0.05 m^3. In order to explore the geometric parameters effects on the overall heat exchanger performance, the performance evaluation criterion (Eq.28) is considered. Indeed, the higher P_{EC} is, the better the overall performance of the heat exchanger.

According to equations 26, 27 and 28, it can be noticed that the performance evaluation criterion is maximal when $S_T/D= S_L/D=1$. Thus, considering the most available sizes in the market, five geometric configurations are compared with the

baseline configuration in order to investigate the achieved air outlet temperature.

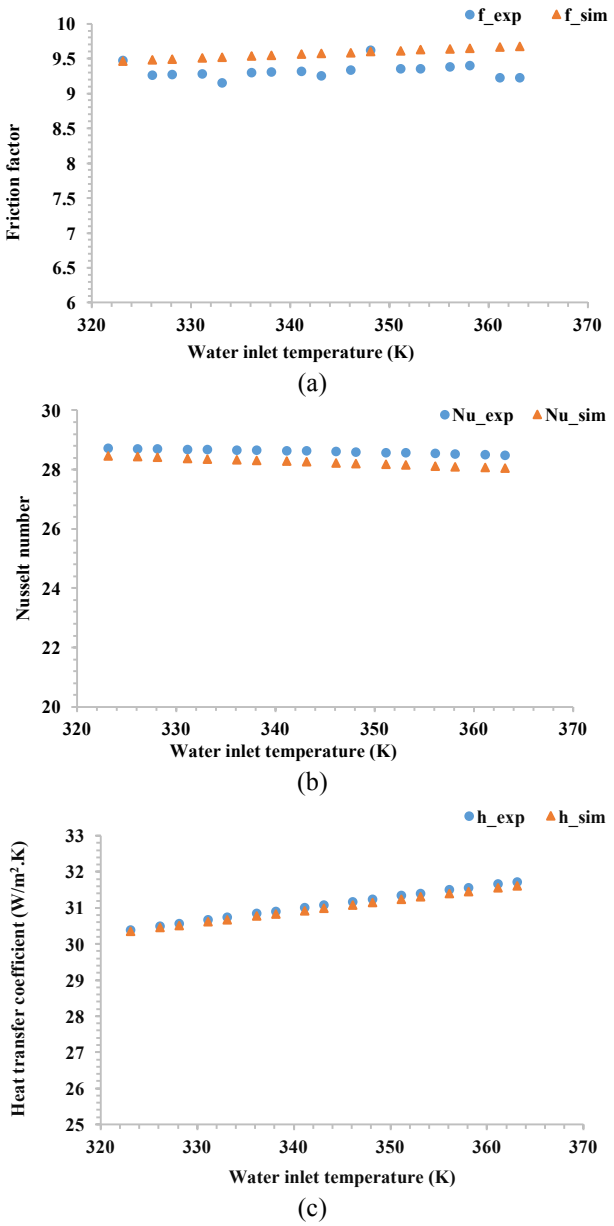

Fig. 8: Influence of water inlet temperature variation on (a) friction factor (b) Nusselt number and (c) heat transfer coefficient

The considered configurations are listed in Table 4 with the corresponding number of tubes per row that is increased in order to keep a constant heat transfer volume when the diameter, transverse pitch and longitudinal pitch dimensions are reduced.

The estimation of the air outlet temperature and performance evaluation criterion of different configurations is illustrated in Fig.9 for a constant fin thickness and fin spacing of 0.3mm and 3.2mm respectively. It can be noticed that the performance evaluation criterion is maximal when the considered geometric parameters are equal to 35mm. However, the air outlet temperature is maximal when the parameters are equal to 18mm. Moreover, the baseline configuration utilization gives the lowest outlet air temperature and performance evaluation criterion that can be enhanced by considering one of the two previous configurations.

The heat exchanger performances are enhanced by around 111.73% where the air outlet temperature is increased by 3.71% when 35mm configuration is considered, while the performances are improved by 53.24% leading the air outlet temperature rise by 9.85% when $D=S_T=S_L=18$ mm.

Despite the higher air outlet temperature improvement rate of 18 mm configuration compared to 35 mm, the performance evaluation criterion obtained by this last configuration remains higher due to the resulting higher pressure drop across the 18mm configuration as shown in Fig. 10.

The estimation of the required transmitted power to the air to overcome the pressure drop across different configurations is illustrated in Fig.10 and shows that for 35mm configuration, 0.91 W has to be transmitted to achieve 3.71% of air outlet temperature enhancement; whereas an additional 0.35 W leads to 9.85% of improvement using 18mm configuration. It can be concluded from Figures 9 and 10 that according to the performance evaluation criterion and the air outlet temperature the optimal configuration is when tube diameter, transverse and longitudinal pitches are equal to 18mm.

Another factor that encouraged this choice is the declining decrease rate of the air outlet temperature provided by 18mm configuration due to the increase of the air velocity compared to 35mm configuration.

The variation effect of the air velocity on the outlet air temperature and the required transmitted power to the air to overcome the pressure drop are presented in Fig. 11. It can be noticed that, based on geometric parameters of 35mm, the air outlet temperature is reduced by around 66.9 %, while with tube bundles of 18mm, the air outlet temperature decreases by only 26.3 % (if the blower delivers to the air a maximal additional power of 36.8 W).

The next step is to optimize the fin spacing and fin thickness for the optimal configuration $D=S_T=S_L=18$mm based on the air outlet temperature. For a constant heat transfer volume, the air outlet temperature has been calculated for F_S = 2 - 3.4mm leading the decrease of the fin thickness for a constant number of fins that remains at its baseline value. As it is shown in Fig. 12, the air outlet temperature is maximal at a fin spacing of 2.9mm and a fin thickness of 0.6mm.

Finally, it can be concluded that the optimal configuration of the considered heat exchanger for a constant heat transfer volume is tubes diameter, transverse and longitudinal pitches of 18mm, 2.9mm of fins spacing, 0.6mm of fins thickness and 11 tubes per row.

Table 4: Number of tubes per row by configuration

Configuration	Number of tubes per row
D=25mm; $S_T=S_L$=35mm	6
$D=S_T=S_L$=35 mm	6
$D=S_T=S_L$=25 mm	8

$D=S_T=S_L=22$ mm	9
$D=S_T=S_L=20$ mm	10
$D=S_T=S_L=18$ mm	11

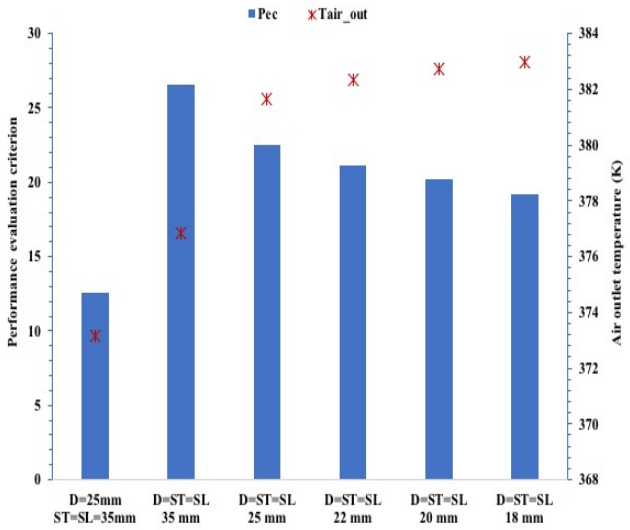

Fig. 9: Comparison of performance evaluation criterion and air outlet temperature for different configurations

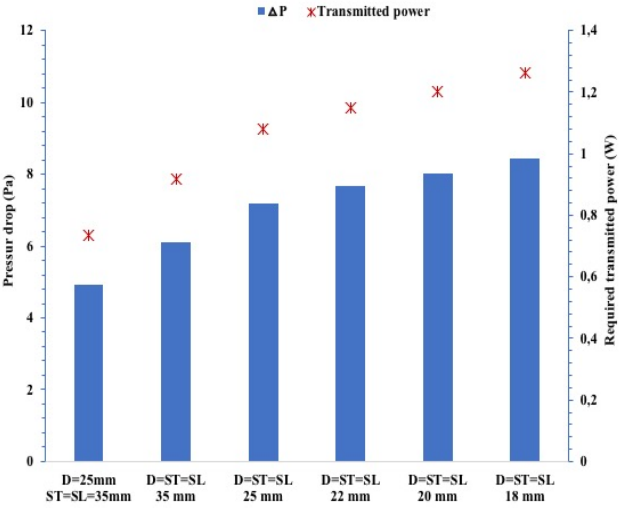

Fig. 10: Comparison of pressure drop and required transmitted power for different configurations

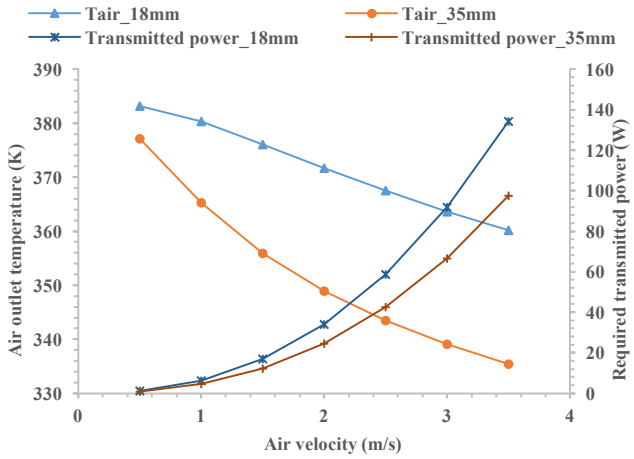

Fig. 11: Variation influence of the air velocity on the required transmitted power and air outlet temperature for 18mm and 35mm configurations

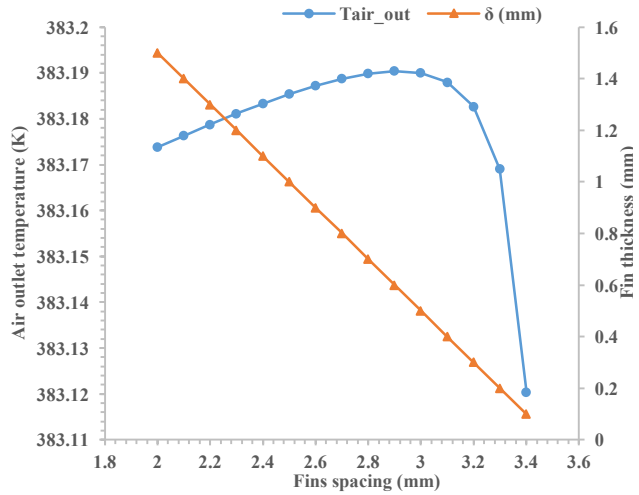

Fig. 12: Variation of the air outlet temperature and fins thickness with fins spacing

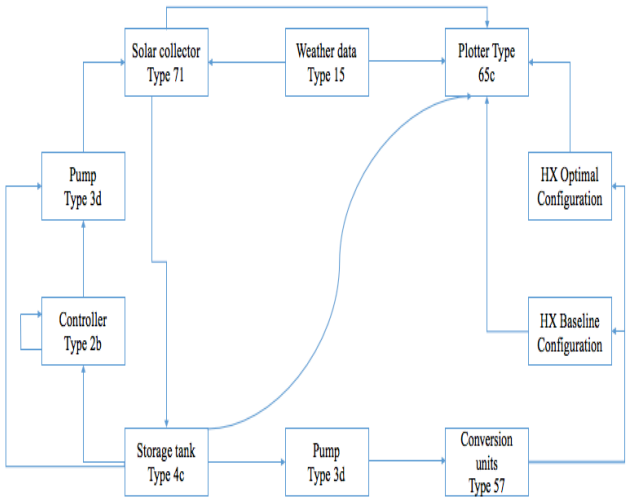

Fig. 13: TRNSYS diagram relative to the solar drying system

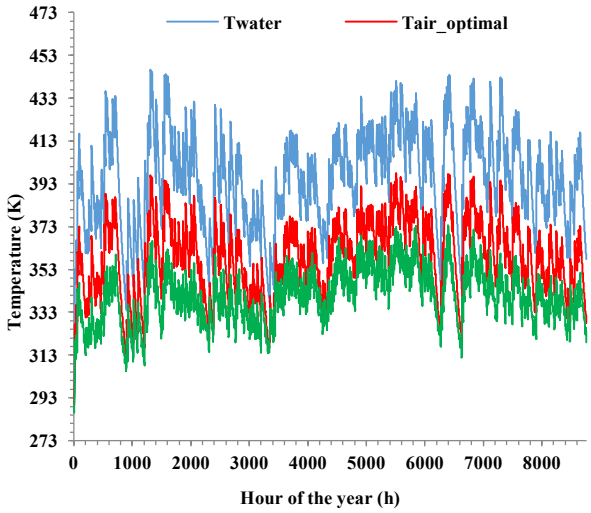

Fig. 14: Annual thermal performance of solar drying system

In order to assess the overall thermal performance of the considered solar drying system under Fez's (center Morocco) climatic condition, the air outlet temperatures provided by the optimal and the baseline heat exchanger configurations have to be simulated and compared. For this purpose, we have considered TRNSYS'17 as its one of the widely used software for transients thermal systems simulation [34-37].

The thermal simulation diagram is displayed in Fig.13 where, the different components of the solar drying system are represented. In fact, Type 71 is used for the modeling of evacuated tube solar collector with an area of 10 m^2 while a hot water storage tank of 200 liters is simulated by Type 4c. The heat regulation system is assured by Type 2b which controls the water pump (Type 3d) to start the circulation of a water flow rate (0.5 kg/s) when the temperature difference between the thermal storage tank is greater than the upper dead band temperature and stop it when it is lower than the lower dead band temperature. Additionally, the modeling of the heat exchanger is performed trough a Matlab code coupled as an external program to TRNSYS. The hourly variations of different temperatures during one year such as the water inlet temperature coming to the heat exchanger from the accumulation tank as well as the air outlet temperatures provided by the optimal and baseline configurations are displayed in Fig. 14. As it can be seen, the air outlet temperature provided by the optimal configuration is, on average, 16% higher than the baseline configuration. This comparison demonstrates the importance of such design optimization in the enhancement of the thermal performances of a solar drying system.

4. Conclusion

With the aim to ensure an efficient design of an industrial clay bricks solar dryer system, modeling and design optimization of a four-row alternant slotted fin-and-tube water to air heat exchanger have been conducted.

- In order to conduct the design optimization, the heat transfer and fluid flow characteristics of the heat exchanger at variable hot fluid inlet temperature have been modeled and validated experimentally. The considered physical model has shown a reliability of more than 99.8% and 97.1%, respectively, for the air outlet temperature and pressure drop.
- According to the conducted experimental investigation, it has been shown that the convective heat transfer increases with increasing the water inlet temperature, while the pressure drop decreases.
- The performed parametric optimization has recommended a tube bundles configuration with tubes diameter, transverse and longitudinal pitches of 18 mm, fins spacing of 2.9 mm and fins thickness of 0.6 mm within the scope of investigation for:

$$1 \le S_T/D \le 1.8 \qquad 1 \le S_L/D \le 1.8,$$
$$2 \le F_s \le 3.4 \qquad 0.1 \le \delta \le 1.5$$
$$800 \le Re \le 13000$$

- The recommended configuration provides a performance evaluation criterion of 19.29 that represents an improvement of 53.21% compared to the one given by the baseline configuration (ST=SL=35mm, D=25mm, δ =0.3mm, FS=3.2mm) that is around 12.53.
- The dynamic simulation of the annual thermal performances of the studied industrial solar dryer system has shown that the recommended configuration enhances the air outlet temperature by more than 16% and consequently contributes to energy saving by improving the whole system efficiency.

Acknowledgements

The authors acknowledge the facilities, and the scientific and technical assistance of the Key Laboratory of Condition Monitoring and Control for Power Plant Equipments of Ministry of Education, School of Energy Power and Mechanical Engineering, North China Electric Power University, Beijing, China. Authors would like to warmly thank all laboratory members for their technical support and availability.

5. References

[1] V. Belessiotis and E. Delyannis, "Solar drying", Solar Energy, vol. 85, pp. 1665–1691, 2009.

[2] G. Pirasteh, R. Saidur, S. M. A. Rahman and N. A. Rahim. "A review on development of solar drying applications", Renewable and Sustainable Energy Reviews, vol. 31, pp. 133–148, 2014.

[3] L. Bennamoun, A. Belhamri, "Design and simulation of a solar dryer for agriculture products", Journal of Food Engineering, vol. 59, pp. 259–66, 2003.

[4] Brick Industry Association, "*Manufacturing of brick. Thechnical notes on brick construction"*, Available from:{http://gobrick.com/portals/25/docs/technical%20notes/tn9.pdf}, 2006.

[5] B. Boutaghriout, C. Hamouda, H Smadi, A. Malek, "Theoretical and experimental investigation of solar heat potential at low temperatures: Towards large scale integration in the agro-food sector", International Journal

of Renewable Energy Research, Vol. 6, No.1, pp. 343-349, 2016.

[6] M. Akoy, M. A. Ismail, E. F. A. Ahmed, and W. Luecke, "Design and construction of a solar dryer for mango slices". Proceedings of International Research on Food Security, Natural Resource Management and Rural Development-Tropentag. University of Bonn, Bonn, Germany, 2006.

[7] N. Mehrdadi, T. Nasrabadi, H. Hoveydi, and S. Joshi,. "Application of solar energy for drying of sludge from pharmaceutical industrial waste water and probable reuse", 2007.

[8] Machine SD Developing a solar drying machine for agricultural products n.d.

[9] A. A. El-Sebaii and S. M. Shalaby, "Solar drying of agricultural products: A review", Renewable and Sustainable Energy Reviews, vol. 16, no. 1, pp. 37–43, Jan. 2012.

[10] G. H. Lee, "A study for the use of solar energy for agricultural industry-solar drying system using evacuated tubular solar collector and auxiliary heater", Journal of Biosystems Engineering, vol. *38,* no.1, pp. 41-47, 2013.

[11] G. Pirasteh, R. Saidur, S. M. A. Rahman, and N. A. Rahim, "A review on development of solar drying applications", Renewable and Sustainable Energy Reviews, vol. 31, pp. 133–148, Mar. 2014.

[12] A. Hubackova, I. Kucerova, R. Chrun, P. Chaloupkova, and J. Banout, "Development of Solar Drying Model for Selected Cambodian Fish Species", The Scientific World Journal, vol. 2014, pp. 1–10, 2014.

[13] A. G. M. B. Mustayen, S. Mekhilef, and R. Saidur, "Performance study of different solar dryers: A review", Renewable and Sustainable Energy Reviews, vol. 34, pp. 463–470, Jun. 2014.

[14] G. Yuan, L. Hong, X. Li, L. Xu, W. Tang, and Z. Wang, "Experimental Investigation of a Solar Dryer System for Drying Carpet", Energy Procedia, vol. 70, pp. 626–633, May 2015.

[15] I. Montero, M. Miranda, F. Sepúlveda, J. Arranz, C. Rojas, and S. Nogales, "Solar Dryer Application for Olive Oil Mill Wastes", Energies, vol. 8, no. 12, pp. 14049–14063, Dec. 2015.

[16] M. Liu, S. Wang, and K. Li, "Study of the Solar Energy Drying Device and Its Application in Traditional Chinese Medicine in Drying", International Journal of Clinical Medicine, vol. 06, no. 04, pp. 271–280, 2015.

[17] M. Kumar, S. K. Sansaniwal, and P. Khatak, "Progress in solar dryers for drying various commodities", Renewable and Sustainable Energy Reviews, vol. 55, pp. 346–360, Mar. 2016.

[18] M. Bououd, O. Hachchadi, K. Janusevicius, A. Mechaqrane, and V. Martinaitis, "Energy performance of a clay tiles solar drying system", In AIP Conference Proceedings, 2056, 020014. AIP Publishing, 2018.

[19] A. Fadhel, K. Charfi, M. Balghouthi, and S. Kooli, "Experimental investigation of the solar drying of Tunisian phosphate under different conditions", Renewable Energy, vol. 116, pp. 762–774, Feb. 2018.

[20] M. Bououd and A. Mechaqrane, "Concentration solar dryer water-to-air heat exchanger: Modeling and parametric studies", International Journal of Hydrogen Energy, vol. 42, no. 13, pp. 8631–8643, Mar. 2017.

[21] M. Bououd, O. Hachchadi, and A. Mechaqrane, 'Plate flat finned tubes heat exchanger: Heat transfer and pressure drop modeling', IOP Conference Series: Earth and Environmental Science, vol. 161, p. 012001, Jun 2018.

[22] J. Zhou and W. Tao, "Three dimensional numerical simulation and analysis of the airside performance of slotted fin surfaces with radial strips", Engineering Computations, vol. 22, no. 8, pp. 940–957, Dec. 2005.

[23] Y. Wang, Y.-L. He, D.-H. Mei, and W.-Q. Tao, "Optimization design of slotted fin by numerical simulation coupled with genetic algorithm", Applied Energy, vol. 88, no. 12, pp. 4441–4450, Dec. 2011.

[24] H. Li, H. Wang, M. Yao, L. Zhang, H. Gu, and J. Nie, "PIV and thermal-vision experimental and numerical investigation on the airside performance of slotted fin surfaces", International Journal of Heat and Mass Transfer, vol. 82, pp. 568–580, Mar. 2015.

[25] Y. Q. Kong, L. J. Yang, X. Z. Du, and Y. P. Yang, "Effects of continuous and alternant rectangular slots on thermo-flow performances of plain finned tube bundles in in-line and staggered configurations", International Journal of Heat and Mass Transfer, vol. 93, pp. 97–107, Feb. 2016.

[26] Y. Q. Kong, L. J. Yang, X. Z. Du, and Y. P. Yang, "Air-side flow and heat transfer characteristics of flat and slotted finned tube bundles with various tube pitches", International Journal of Heat and Mass Transfer, vol. 99, pp. 357–371, Aug. 2016.

[27] VDI e. V., Ed., VDI Heat Atlas. Berlin, Heidelberg: Springer Berlin Heidelberg, 2010.

[28] S. E. Haaland, "Simple and Explicit Formulas for the Friction Factor in Turbulent Pipe Flow", Journal of Fluids Engineering, vol. 105, no. 1, p. 89, 1983.

[29] T. E. Schmidt, "Heat transfer calculations for extended surfaces", Refrigerating Engineering, vol. 57, no 4, p. 351-357, 1949.

[30] C.-C. Wang and C.-T. Chang, "Heat and mass transfer for plate fin-and-tube heat exchangers, with and without hydrophilic coating", International Journal of Heat and Mass Transfer, vol. 41, no. 20, pp. 3109–3120, Oct. 1998.

[31] C.-C. Wang, K.-Y. Chi, and C.-J. Chang, "Heat transfer and friction characteristics of plain fin-and-tube heat exchangers, part II: Correlation", International Journal of Heat and Mass Transfer, vol. 43, no. 15, pp. 2693–2700, Aug. 2000.

[32] Keysight 34970A/34972A Data Acquisition/Switch Unit Service Guide 34972-90010 Edition 4, August 2014.

[33] R. J. Moffat, "Describing the uncertainties in experimental results", Experimental Thermal and Fluid Science, vol. 1, no. 1, pp. 3–17, Jan. 1988.

[34] C. Naranjo-Mendoza, D. R. Rousse, and G. Quesada, 'Modeling of a solar absorption cooling system for Guayaquil, Ecuador', in 2013 International Conference

on Renewable Energy Research and Applications, Madrid, Spain, 2013, pp. 853–856.

[35] M. Asma and T. Youssef, 'Modeling of The Parabolic trough Solar Field with Molten Salt for The Region of Tozeur in Tunisia', in 2018 7th International Conference on Renewable Energy Research and Applications, Paris, 2018, pp. 993–997.

[36] M. H. Ahmed, A. Giaconia, and A. M. A. Amin, 'Effect of solar collector type on the absorption system performance', in 2017 IEEE 6th International Conference on Renewable Energy Research and Applications, San Diego, CA, 2017, pp. 304-309.

[37] M. Bououd, O. Hachchadi, K. Janusevicius, V. Martinaitis, and A. Mechaqrane, 'Solar air heating system: design and dynamic simulation', IOP Conference Series: Materials Science and Engineering, vol. 353, p. 012004, May 2018.

[38] ⟨http://ship-plants.info/solar-thermal-plant (Last accessed: 09/06/2019)